Princeton Plasma Physics Laboratory

PPPL- 4516

PPPL- 4516

# Intermittent Divertor Filaments in the National Spherical Torus Experiment and Their Relation to Midplane Blobs

R.J. Maqueda, D.P. Stotler and the NSTX Team

May, 2010

Prepared for the U.S. Department of Energy under Contract DE-AC02-09CH11466.

# Princeton Plasma Physics Laboratory
# Report Disclaimers

---

## Full Legal Disclaimer



## Trademark Disclaimer



---

# PPPL Report Availability

## Princeton Plasma Physics Laboratory:

http://www.pppl.gov/techreports.cfm

## Office of Scientific and Technical Information (OSTI):

http://www.osti.gov/bridge

---

**Related Links:**

**U.S. Department of Energy**

**Office of Scientific and Technical Information**

**Fusion Links**

Nucl. Fusion **50** (2010) 000000 (12pp) UNCORRECTED PROOF

# Intermittent divertor filaments in the National Spherical Torus Experiment and their relation to midplane blobs

**R.J. Maqueda[1], D.P. Stotler[2] and the NSTX Team[a]**

[1] Nova Photonics, Inc., Princeton, NJ 08540, USA
[2] Princeton Plasma Physics Laboratory, Princeton, NJ 08543, USA

E-mail: rmaqueda@pppl.gov

Received 4 March 2010, accepted for publication 6 May 2010
Published
Online at stacks.iop.org/NF/50

**Abstract**
While intermittent filamentary structures, also known as blobs, are routinely seen in the low-field-side scrape-off layer of the National Spherical Torus Experiment (NSTX) (Ono *et al* 2000 *Nucl. Fusion* **40** 557), fine structured filaments are also seen on the lower divertor target plates of NSTX. These filaments, not associated with edge localized modes, correspond to the interaction of the turbulent blobs seen near the midplane with the divertor plasma facing components. The fluctuation level of the neutral lithium light observed at the divertor, and the skewness and kurtosis of its probability distribution function, is similar to that of midplane blobs seen in $D_\alpha$; e.g. increasing with increasing radii outside the outer strike point (OSP) (separatrix). In addition, their toroidal and radial movement agrees with the typical movement of midplane blobs. Furthermore, with the appropriate magnetic topology, i.e. mapping between the portion of the target plates being observed into the field of view of the midplane gas puff imaging diagnostic, very good correlation is observed between the blobs and the divertor filaments. The correlation between divertor plate filaments and midplane blobs is lost close to the OSP. This latter observation is consistent with the existence of 'magnetic shear disconnection' due to the lower X-point, as proposed by Cohen and Ryutov (1997 *Nucl. Fusion* **37** 621).

**PACS numbers:** 52.35.Ra, 52.55.Rk, 52.40.Hf, 52.55.Fa, 52.70.Kz

S Online supplementary data available from stacks.iop.org/NF/50/1/mmedia

AQ1 (Some figures in this article are in colour only in the electronic version)

## 1. Introduction

Intermittent filamentary structures are routinely seen on the outboard edge of magnetically confined fusion experiments. These coherent structures, most commonly named 'blobs' [1, 2] but also known as intermittent plasma objects (IPOs) [3], avaloids [4] or just inter-edge localized mode (ELM) filaments [5–8], have been shown to contribute up to 50% of the cross-field transport [3] and result in relatively flat profiles for the far scrape-off layer (SOL) on the outer, low-field-side edge region of these experiments [9]. The theoretical interpretation for the propagation of blobs in the SOL is that charge separation within the filament's plasma due to non-ambipolar drifts, such as curvature or $\nabla B$ drifts, gives rise to a local electric field that then results in the radial outward movement of the blobs due to $\boldsymbol{E} \times \boldsymbol{B}$ drift [10]. The blob filaments, as observed experimentally, move outwards reaching the plasma facing components of the device. The charge separation within the blob filament, which governs its radial velocity, is maintained by the electrical resistivity, both along the filament length and at the filament ends, either a plasma sheath on a material surface or a dense plasma region such as the magnetic X-point region [11].

In this paper we present data from the National Spherical Torus Experiment (NSTX) [12] showing that intermittent filamentary structures are also seen on the lower divertor target plates of the device. These filaments are similar to those observed during ELMs [13], but are not related to them since they are seen during inter-ELM periods. Furthermore, as shown in this paper, they correspond to the interaction, or footprint, on the target plate of the field-aligned blob filaments seen near the outboard midplane of NSTX [2]. Intermittent (i.e. non-Gaussian) fluctuation has been previously observed in the divertor region of other experiments [14–15] and long

[a] See author list of D.A. Gates *et al* 2009 *Nucl. Fusion* **49** 104016.

 

JNL: NF PIPS: 350265 TYPE: PAP TS: NEWGEN DATE: 18/5/2010 EDITOR: MJ

correlation lengths have been inferred for fluctuations in the SOL of JET, connecting for instance lower divertor Langmuir probes with probes on plasma facing components on the top of the device [16]. Nevertheless, it is believed that this is the first time that the connection has been made between divertor intermittent fluctuations with midplane intermittent fluctuations (i.e. blobs). Consequently, in a similar way that midplane blobs can result in plasma reaching plasma facing components in the main chamber [17], the blob footprints in the divertor can result in particles and energy reaching unarmoured far-SOL regions of the divertor. Nevertheless, the contribution that the blobs have to the heat and particle deposition profiles on the divertor target plates is not described in this paper, leaving such an analysis for a subsequent publication.

This paper is organized as follows. The NSTX device and the imaging diagnostics used for the measurements presented are described in section 2. In section 3, the measurements are described, first giving a characterization of the observations made on the divertor target plates and then relating these observations to blobs observed in the midplane with the gas puff imaging (GPI) diagnostic. The paper concludes in section 4 with a brief summary and discussion of the results.

## 2. Experimental setup

The measurements described in this paper were obtained in the NSTX [12]. This experiment is a low aspect ratio tokamak with a major radius $R = 0.86$ m and a minor radius $a = 0.67$ m. A plasma current $I_p = 0.9$–$1.0$ MA, a toroidal field on axis $B_t = 0.45$–$0.55$ T, an elongation $\kappa \sim 2.2$ and a lower triangularity $\delta_{bot} = 0.7$–$0.8$ were used in a lower single null configuration with the distance between the lower (primary) and upper (secondary) X-points, mapped to the outboard midplane, $\delta R_{sep} = 1$–$1.5$ cm. The NSTX device has an open divertor configuration with the inner and outer target plate covered in carbon tiles. Nevertheless, the inner strike and outer strike points (OSPs) were, respectively, located on the vertical central column and on the inner divertor target plate. Plasmas in high confinement mode (H-mode) were used, heated by 6 MW of neutral beam injection. Although ELMs were present on some of these discharges, inter-ELM periods were used for the work presented here.

The main diagnostic used in the work presented in this paper was high frame rate imaging in the visible range of wavelengths. Three fast-framing digital cameras were employed with different views of the plasma, all three coupled to the device through coherent imaging bundles. The first camera, a Phantom 7.3 from Vision Research, viewed the divertor target surfaces from above and was run at 88 888 frames $s^{-1}$, yielding an inter-frame time of 11.25 $\mu$s. A Li I interference filter with its central wavelength at 670.8 nm and a 1.5 nm bandwidth were located between the imaging bundle and the camera. The plasma facing components in NSTX are coated with a thin layer of lithium deposited by a pair of evaporators [18]. This coating provided a source of neutral lithium which, due to its low ionization energy of 5.4 eV, resulted in the Li I light originating from within 2 cm from the target plates being imaged. Figure 1 shows the field of view (FOV) of this camera. In figure 1(*a*) the centre stack, inner divertor target plate, outer divertor target plate and bottom passive stabilizing plate can be seen. This image of the vessel interior is obtained in the absence of plasma with an in-vessel illumination filament that is partially shadowed by the centre stack. The inner divertor and outer divertor, on the other hand, are separated by a 4.5 cm gap used for coaxial helicity injection experiments [19] and hence termed the 'CHI gap' in this paper. Figure 1(*b*) shows an image obtained from the average of many individual frames captured with the Li I filter during a plasma discharge. Each individual image from the top-down viewing camera is exposed for 9.25 $\mu$s.

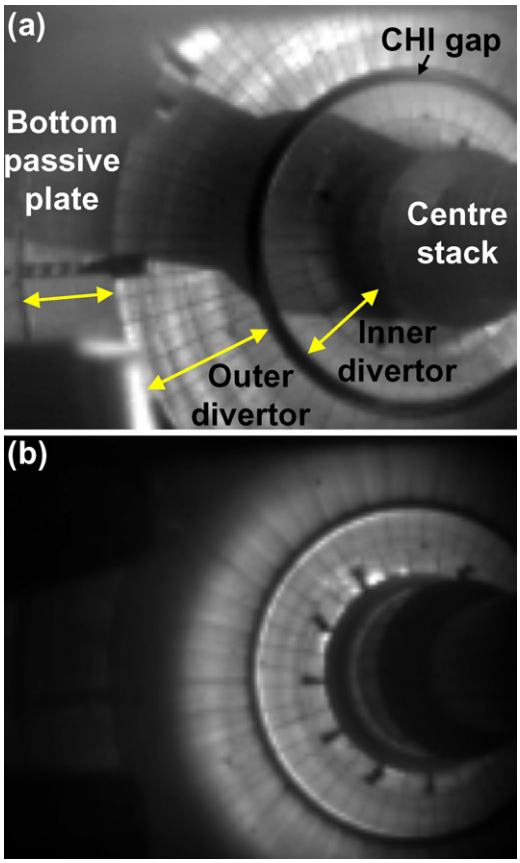


**Figure 1.** FOV of the top-down viewing camera: (*a*) with in-vessel filament illumination (no interference filter), (*b*) average image from 6223 individual frames obtained during a 70 ms-long ELM-free period (shot 124750, 410 ms to 480 ms) using the Li I filter. The centre stack, inner divertor, CHI gap, outer divertor and bottom passive plate are identified in part (*a*).

The second camera (a Phantom 7.1) was used in the GPI diagnostic and viewed a tangential ~25 cm poloidal section of the edge just above the outer midplane of the plasma [20]. This camera was run at 117 647 frames $s^{-1}$ (8.5 $\mu$s inter-frame time) and 5 $\mu$s exposures. The pitch angle of the magnetic field in the viewing region of this tangential edge camera was selected so that the visible light emission was viewed along the direction of the local magnetic field line. In this way, 'end-on' images of the field-aligned edge structure and filaments were obtained. In addition, a non-perturbing deuterium gas puff (~10 Torr l $s^{-1}$) was added in the FOV of the GPI camera to further localize the emitting region to a ~20 cm length along the line of sight and also increase the contrast and brightness of the $D_\alpha$ line emission which was selected with a narrow-band interference filter. DEGAS 2 simulation of the $D_\alpha$ emission in this diagnostic setup indicates that the spatial

structure of the emitting neutral cloud captured in the camera images reflects the 2D structure of the turbulence, despite a non-linear dependence of the emission on the electron density and temperature of this plasma [21]. Further details of this GPI diagnostic, as well as of the non-perturbing condition of the gas puff itself, can be seen in [2, 20].

The third camera, also a Phantom 7.3, was used in a tangential view of the lower divertor [22], imaging mainly the inner divertor target plate and having a higher spatial resolution of this region than the top-down viewing camera. This tangential viewing camera was run with the same framing rate, exposure and Li I interference filter as the first (top-down) Phantom 7.3 camera. These two cameras were frame-synchronized to each other using their onboard 'master/slave' capability. The GPI camera, although running independently and at a faster frame rate, was checked to have its time-base accurate to within $\pm 10\,\mu$s relative to the Phantom 7.3 time-base. This maximum possible mismatch of $10\,\mu$s represents no more than one frame of the Phantom 7.3 image sequence.

The dependence on the electron density $n_e$ and electron temperature $T_e$ of the spectral line being observed, the $2p^2P^0 \rightarrow 2s^2S$ transition of neutral lithium at 670.78 nm, is dominated by a linear relationship with $n_e$. The line emission can be written as

$$I = n_e n_{Li} f_{Li^\circ}(\mathrm{PEC}), \qquad (1)$$

where $n_{Li}$ is the total density of lithium atoms and ions in all charge states, $f_{Li^\circ}$ is the fraction abundance of the $Li^{0+}$ (i.e. neutral) in its ground state and PEC is the photon emission coefficient (photons $m^3\ s^{-1}$). This coefficient is obtained from the collisional–radiative ADAS database, including excitation, ionization and recombination cross-sections for states up to $n = 4$ and generalized states with $n < 500$ [23]. The $n_{Li}$, $f_{Li^\circ}$ and PEC factors in equation (1) are, under the conditions of the measurements, weaker functions of $n_e$ and $T_e$ than the explicit $n_e$ linear dependence.

The filaments being observed are transient events with characteristic timescales of $\sim 50\,\mu$s (section 3.1). Within this short timescale it can be assumed that the total lithium density ($n_{Li}$) is constant in time. At the same time the fractional abundance $f_{Li^\circ}$, although evolving due to changes in $n_e$ and $T_e$, does not have enough time to change towards the new collisional–radiative equilibrium imposed by this change in $n_e$ and $T_e$. It can be noted that at densities of $< 10^{19}\,m^{-3}$, it takes in at least 2 ms for low-$Z$ impurities to reach within 1% of the new steady-state populations [24]. Finally, the PEC calculated under the collisional–radiative model (figure 2) is only weakly dependent on $n_e$ and $T_e$ within the density range $10^{16} < n_e < 10^{18}\,m^{-3}$ and $T_e > 5$ eV. In summary, in the short filament timescale the line emission responds linearly to changes in the electron density and it has a weaker-than-linear dependence on the electron temperature. (In the 1–4 eV range, for the lowest densities, the temperature dependence is close to linear.)

## 3. Filamentary emission in the divertor

An example of the lower divertor filaments can be seen in figure 3. The images in this figure, covering a total period of 225 $\mu$s, have been obtained with the top-down viewing camera using a Li I bandpass filter and the same FOV as that shown in figure 1. The discharge shown had $\kappa \sim 2.4$, $\delta_{bot} \sim 0.8$ and the OSP was located at $R \sim 34$ cm, indicated with a dashed line in figure 3. The inner strike point is located on the 28 cm radius centre stack, ~11 cm above the inner target plate. As pointed out in the preceding section, these images correspond to an ELM-free period during an H-mode discharge. It should be noted that in images that would be otherwise obtained using long frame exposures, the very many filaments present during such long periods result in the smearing out of this short-timescale structures, as seen in the average image shown in figure 1(*b*).

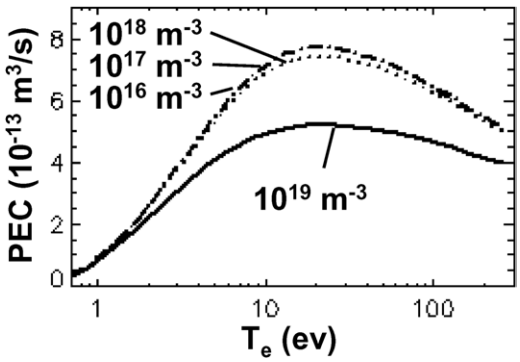


**Figure 2.** PEC for the Li I 670.8 nm emission line. Data from the collisional–radiative model, ADAS database. The electron densities are indicated for each trace in this plot.

As can be seen in figure 3, filaments are seen moving toroidally with many filaments present at different radii in each image. Small circles have been added to some of the images in this figure to guide the eye and identify individual filaments moving into these circles. The phenomena shown can be better observed in the *movie*[3] covering 2 ms of the same discharge (596 to 598 ms). The characteristics of these filaments and their movement are presented in section 3.1.

The intersection with the divertor target of a circular midplane magnetic flux tube is shown in the frame #8 of figure 3. This midplane circular flux tube is centred at a normalized poloidal flux $\Psi_N = 1.174$ and has a 3 cm diameter in the cross-field (radial versus poloidal) plane. Due to magnetic shear, as this flux tube reaches the divertor plates, the intercept (or flux tube footprint) has been deformed into a toroidally elongated structure. This is further discussed in section 3.2. The field-line mapping from the midplane to the divertor target plates has been carried out using the equilibrium reconstruction obtained by EFIT [25]. The relation between the divertor filaments shown in figure 3 and midplane intermittent events (blobs) observed with the GPI diagnostic is presented in sections 3.2 and 3.3.

### 3.1. Characteristics of the divertor filaments

As can be seen in figure 3, the divertor filaments are wider at larger radii than at smaller radii. This characteristic can be more clearly observed in figure 4. Part (*a*) of this figure shows the zero-time-lag cross-correlation coefficients ($\rho$) between

[3] http://www.pppl.gov/~rmaqueda/other/temp/paper/nstx_movie_01.avi (38 Mbytes).

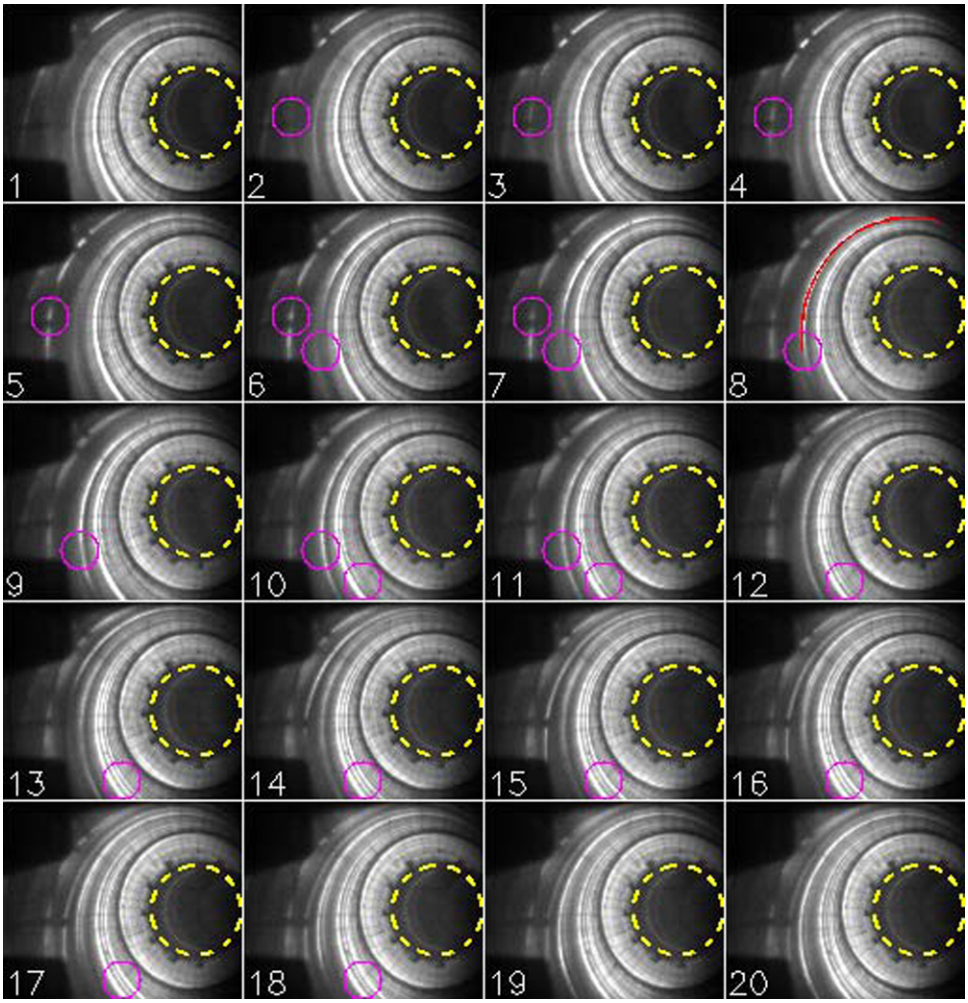


**Figure 3.** Images showing toroidally moving filaments on the lower divertor surfaces of NSTX. The images, covering the period from 596.514 ms (frame #1) to 596.739 ms (frame #20) of shot 124750, are each exposed during 9.25 $\mu$s. No contrast enhancement has been applied to these images, representing the raw neutral lithium emission (670.8 nm) originating in plasma–wall interactions. The dashed line around the centre stack indicates the position of the OSP.

all pixels in the images, from a sequence similar to that in figure 3, with respect to several different reference points indicated with + symbols in these images. The correlation maps in figure 4(*a*) correspond to the same FOV and orientation as the images in figure 3. The reference point positions are indicated in terms of the normalized flux function $\Psi_N$. Very good correlation is maintained along toroidally elongated regions whose width increases with radius. The filaments are also better defined at smaller radii ($\Psi_N < 1.3$) than at larger radii where, although a filament is still observed, there is a broad region surrounding this filament with increased cross correlation relative to the reference point.

The radial profiles of the zero-time-lag cross-correlation (figure 4(*a*)) in a narrow toroidal slice including the reference point are shown in figure 4(*b*). In this case the positions within the divertor target plates and bottom passive stabilizing plate are mapped to the outboard midplane and given as a distance relative to the outboard midplane separatrix position. Nevertheless, a secondary abscissa axis in terms of $\Psi_N$ is also provided on top of figure 4(*b*). Close to the separatrix the width of the divertor filament, at a given toroidal angle, is of only a few millimetres when mapped to the midplane. This width should not be confused with the radial extent of the filaments which, due to their spiral shape in contrast with a circular shape, extend further in major radius than the profiles at a fixed toroidal angle indicate. The narrow filament characteristics closer to the separatrix will be further discussed in section 3.2. As pointed out in the preceding paragraph 'wings' develop on the profiles for reference points further away from the separatrix, in addition to them being broader, indicating that the filaments dissipate or lose structure at large radii.

Some of the statistical turbulence characteristics of the neutral lithium emission from the divertor target plates and the bottom passive stabilizing plate are shown in figure 5. These are shown as a function of the distance to the separatrix when mapped to the midplane, similar to figure 4(*b*). The average light level ($I_{\mathrm{Li\,I}}$), root-mean-square fluctuation level ($\delta I/I$ rms), skewness, kurtosis and autocorrelation time ($\tau_{\mathrm{auto}}$) are calculated for each pixel of the raw images during a 70 ms long, ELM-free period. These values are then grouped into toroidal stripes which are 2 cm wide at the divertor, averaged (thick lines) within each group and the standard deviation (thin lines) calculated. The grey band indicates the position of the CHI gap.

The Li I light in figure 5(*a*) starts increasing just outside the OSP, decaying in the far SOL $R_{\mathrm{mid}} - R_{\mathrm{sep}} > 4$ cm. The relative fluctuation level in this emission as shown in figure 5(*b*)

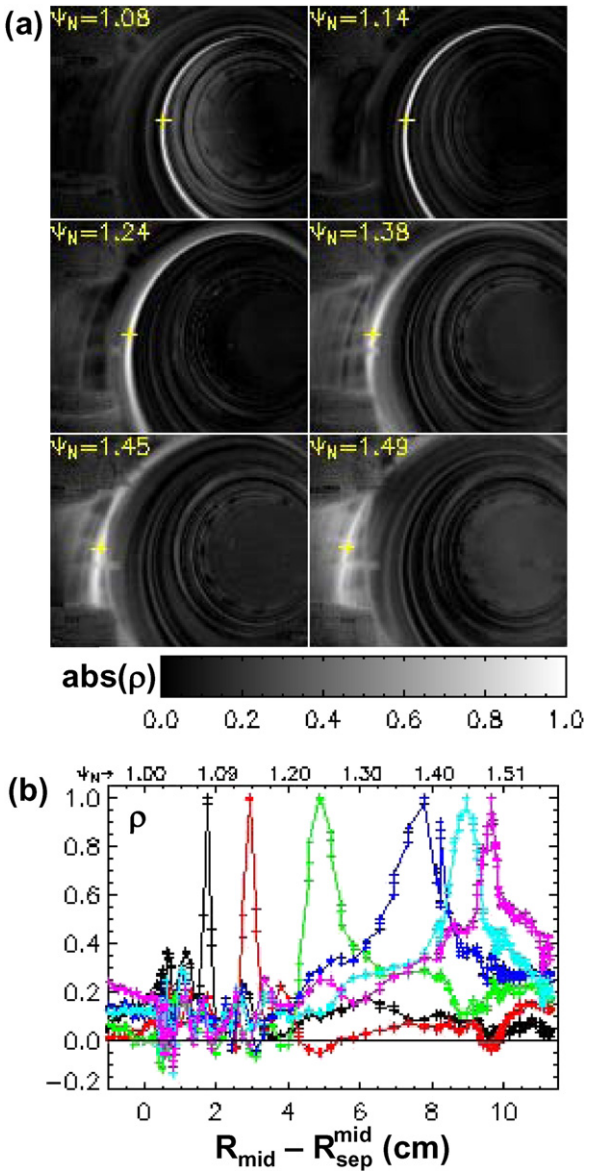


**Figure 4.** Average shape of the divertor filaments obtained from zero-time-lag cross-correlation relative to six different reference points: (*a*) 2D maps of the cross-correlation coefficient ($\rho$) over the same FOV as that shown in figure 3. (*b*) Radial profiles of $\rho$ in narrow toroidal slices containing the six reference points. An ELM-free image sequence from the same shot as in figure 3 is used (from 595 to 615 ms).

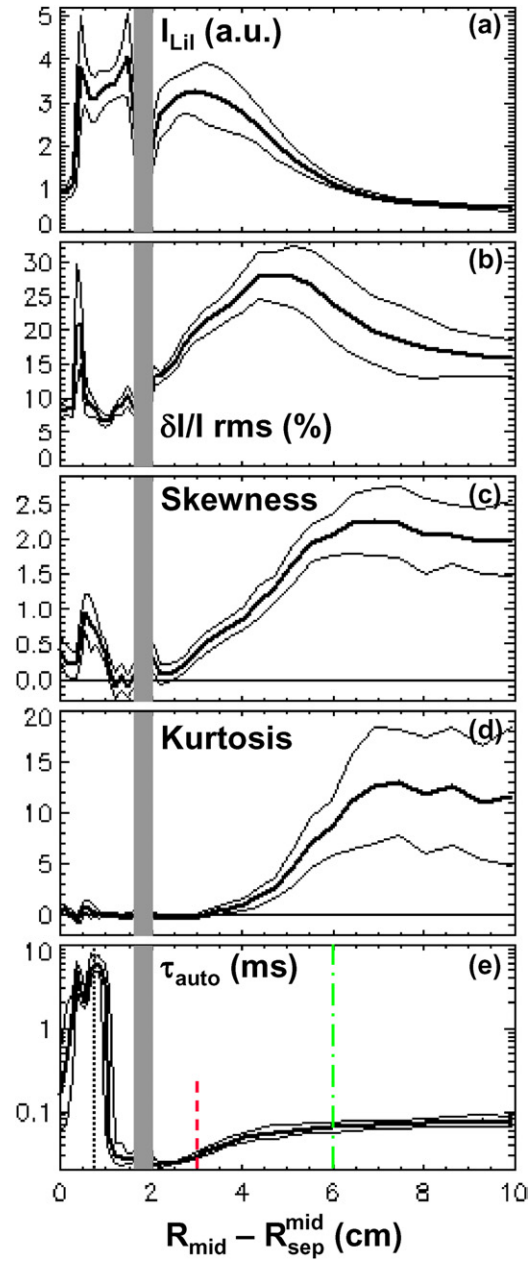


**Figure 5.** Characteristics of the neutral lithium emission observed on the divertor target plates and bottom passive stabilizing plate. The abscissa is the distance to the separatrix when mapped to the outboard midplane. The grey band indicates the position of the CHI gap. In this case the top-down images in the 410 to 480 ms ELM-free period of shot 124750 are used.

is large near the strike point, possibly due to small changes in the strike point position but then stays at a relatively low 10% level up to the CHI gap outside which it increases to a 25–30% level and then slowly decreases in the far SOL. As the fluctuations increase so do the skewness and kurtosis (figures 5(*c*) and 4(*d*), respectively), indicating that these fluctuations have intermittent characteristics. In the far SOL the skewness reaches a level of ∼2 and the kurtosis 10–12, with the increase of the latter starting at larger radii. Finally, in figure 5(*e*), the autocorrelation time is seen to plateau at ∼80 $\mu$s within the SOL, outside of the CHI gap.

The time-delayed autocorrelation function and frequency spectra for the divertor Li I light are shown in figure 6 at three different radii (0.75, 3 and 6 cm, relative to the midplane separatrix). These positions on the divertor target plates are indicated in figure 5(*e*) and correspond to normalized flux function values of 1.03, 1.16 and 1.33, respectively. As can be seen in figure 6 there is a clear difference between close to the separatrix, or OSP, and far away from them. The autocorrelation times shown in figure 5(*e*) are obtained as the half-width at half-maximum (HFHM) values of the corresponding time-delayed autocorrelation functions like those shown in figure 6(*a*). These functions show that away from the separatrix (OSP) there are no long-time correlations, indicating the presence of individual, random events. The FFT amplitude spectra shown in figure 6(*b*) indicate, at the same time, that there are no significant narrow-band modes present and the spectra away from the OSP show a relatively flat profile

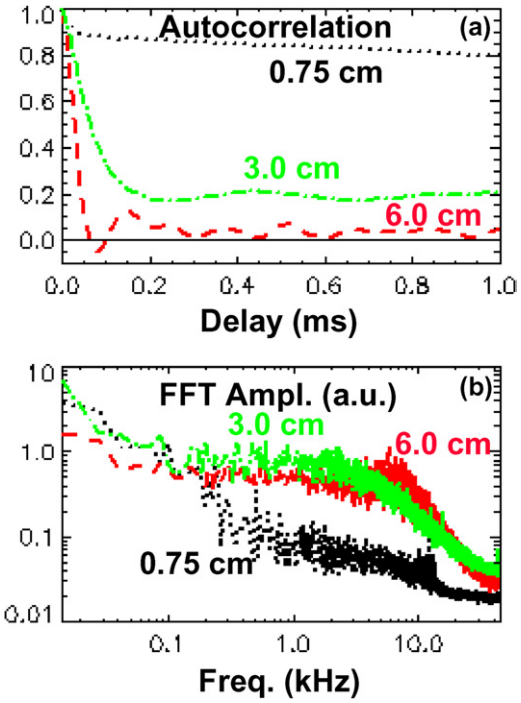


**Figure 6.** Time-delayed autocorrelation functions (*a*) and frequency spectra (*b*) of the neutral lithium emission observed on the divertor target plates and bottom passive stabilizing plate. The distances indicated on these plots are the midplane distance to the separatrix when mapped to the outer midplane. The same image sequence as that used for figure 5 is used here. The frequency spectra in (*b*) have been normalized to have all the same steady-state (0 Hz) amplitude.

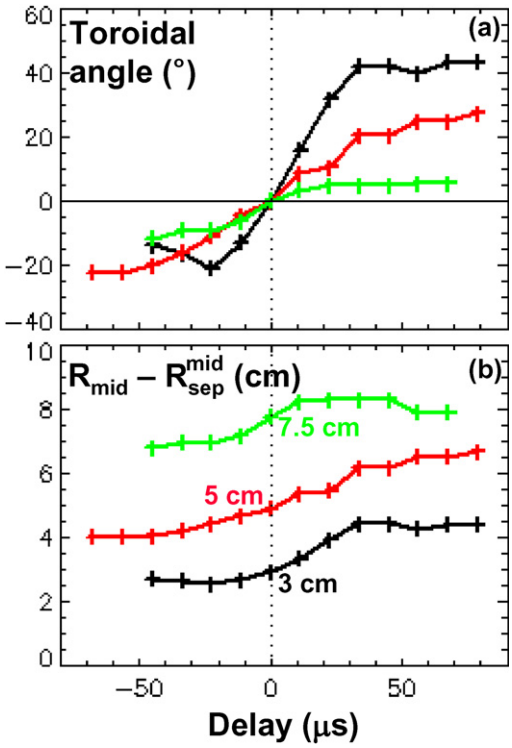


**Figure 7.** Average movement of the filaments observed on the divertor of NSTX. These are obtained from the time-delayed cross-correlation functions as described in the text. Three reference points are used, approximately at 3 cm (black), 5 cm (red) and 7.5 cm (green) outside the separatrix when mapped along field lines to the outboard midplane. The toroidal movement is shown in (*a*) and the radial movement (mapped to the outboard midplane) is shown in (*b*). The same ELM-free image sequence as that in figure 5 is used.

at low frequencies and power-law decay at frequencies higher than a characteristic inflection point at 6–8 kHz. Close to the separatrix (black trace) the high frequency fluctuations appear to be suppressed.

The average movement of the filaments observed on the bottom divertor of NSTX can be obtained from the time-delayed cross-correlation functions. Given a reference point within the image, at any given time delay (either positive or negative) the cross-correlation map between all points in the image and the reference point reach a maximum at some distance from the reference, indicating the average movement of the structures observed. The positions of these maxima for different delay times (abscissa) are shown in figure 7, where only data points with maxima greater than a 65% correlation coefficient are shown. The three reference points used, corresponding to maxima at 0 $\mu$s delay (and 100% correlation), are located at approximately 3, 5 and 7.5 cm outside the separatrix when mapped along field lines to the outboard midplane. The toroidal (figure 7(*a*)) and radial (figure 7(*b*)) movements observed in this figure match well that seen in the movies (i.e. figure 3) when tracking individual filaments. It should be pointed out that due to the 'barber pole effect' when observing a narrow region in toroidal direction, the toroidal movement of toroidally elongated helical structures may appear as a radially inward movement. This will be further discussed in the following section.

Due to the toroidally elongated structure of the filaments, particularly in the case of the furthest inward reference point (black traces in figure 7), the centroid of the filament is not within the FOV of the imaging system and hence the movement cannot be accurately followed at large time delays (in absolute value), even though the correlation relative to the reference point is still relatively good (>65%). The black traces in figure 7 show artificial plateaus at large delays due to this imaging limitation. In the case of the furthest out reference point (green traces in figure 7) the filaments may be partially dissipating as discussed in the context of figure 4(*b*), and their toroidal and radial movements appear to stop when reaching ~8 cm from the separatrix. This is approximately the flux surface of midplane facing components in NSTX.

### *3.2. Relationship to midplane intermittent events*

The fluctuating, moving filaments seen on the divertor target plates and lower stabilizing passive plate described in the preceding section have many similarities to the intermittent events (blobs) seen near the outboard midplane of NSTX. Many of the characteristics of these blobs in NSTX have been presented in [2]. They are ejected from the closed field-line region and propagate both radially outwards and predominantly downwards, the ion diamagnetic drift direction, in the SOL. The normalized root-mean-square fluctuation level, skewness and kurtosis increase away from the separatrix and into the far SOL. These same characteristics are observed in figures 5(*b*)–(*d*) for the filaments observed close to the divertor plasma facing components. In this section, the relationship between the measurements of blobs at the midplane of NSTX using the GPI diagnostics (see section 2) and the divertor filaments is established.

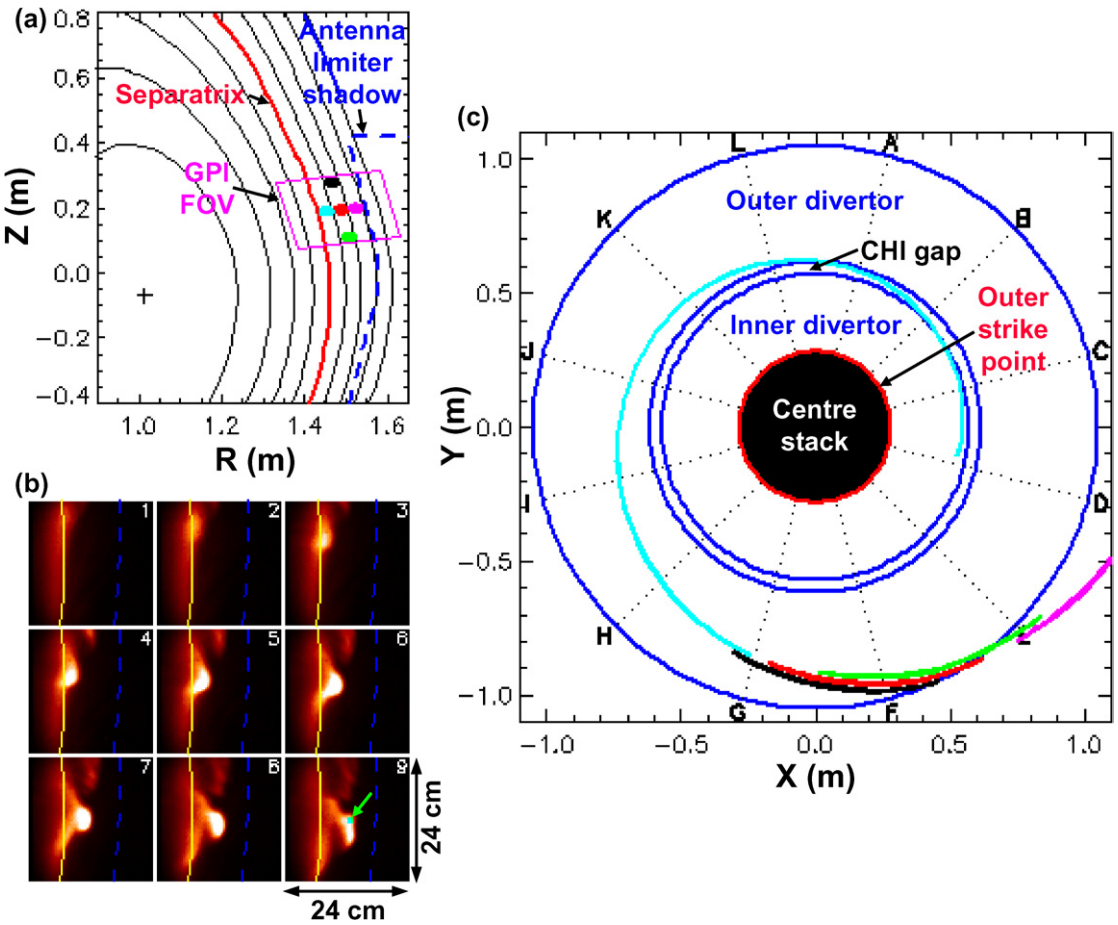


**Figure 8.** The mapping of midplane circular flux tubes results in elongated, narrow structures when intersecting the plasma facing components on the lower divertor region. (*a*) The FOV of the GPI diagnostics is shown on the poloidal cross section of NSTX. (*b*) Sequence of nine consecutive image frames from the GPI diagnostic: shot 130322, from 428.071 ms (top left) to 428.147 ms (bottom right). The deuterium diagnostic gas is injected in a narrow sheath close to orthogonal to the local magnetic field lines. A $D_\alpha$ filter is used in the GPI diagnostic. The separatrix is shown with a solid yellow line and the antenna limiter shadow is indicated with a dashed blue line. (*c*) Mapping to the divertor surfaces of the five colour-coded 3 cm diameter flux tubes shown in (*a*). The letters shown are indicative of the diagnostic bays of the NSTX experiment. The GPI diagnostic is located near the midplane between bays A and B.

The FOV of the GPI diagnostic is identified in the outboard poloidal cross section of NSTX shown in figure 8(*a*). This view, covering an area of 24 cm × 24 cm of the radial versus poloidal cross-field plane is located just above the outer midplane ($Z = 0$) and it generally contains the separatrix and the shadow of the RF antenna limiter. It should be noted here that due to the high pitch angle of the magnetic field line on the outboard region of the NSTX spherical torus, the target plane of the camera is tilted ∼45° with respect to the poloidal plane (i.e. $R$–$Z$). The FOV of the GPI diagnostic is then along the local magnetic field line so as to isolate the cross-field characteristics of the field aligned structures present at the edge. Because of this and the 3D localization provided by the deuterium gas puff, the filamentary turbulent structures appear as blobs in the resulting images. A sequence of nine frames, covering a total time period of ∼75 $\mu$s, is displayed in figure 8(*b*) and shows an example of a blob filament being ejected from the typically quiescent H-mode edge. (The separatrix and shadow of the antenna limiter are indicated with a yellow line and a dashed blue line, respectively.)

As can be seen in figure 8(*b*) the intermittent midplane blobs have a characteristic cross-field dimension of 3–4 cm in both radial and poloidal directions. Making use of the EFIT equilibrium reconstruction the magnetic flux tube occupied by the midplane blob can be mapped to the plasma facing components of the lower divertor region. Five such mappings are shown in figure 8(*c*), each corresponding to a midplane circular region in the true cross-field plane of 3 cm diameter. This is similar to the mapping done in [13] for ELM related filaments and results, due to the magnetic shear and flux expansion, in toroidally elongated, narrow structures when intersecting the plasma facing components. In this case the midplane position of these colour-coded flux tubes is indicated within the GPI FOV in figure 8(*a*). A similar flux tube mapping was shown in frame #8 of figure 3. Similar to figure 3, the shot used here had a high elongation magnetic topology with the OSP located on the inner divertor target plate, in this case within a centimetre from the base of the centre stack.

Following the colour-coded flux tubes of figures 8(*a*) and (*c*) it is then clear that a radially outward movement of midplane blobs (cyan–red–purple) translates into a spiral trajectory for the movement of their divertor footprints when viewed from the top of the machine. Similarly, the downward movement predominantly seen in midplane blobs (black–red–green) corresponds to a toroidal counter clockwise movement when looking into the divertor from above. It is here that it

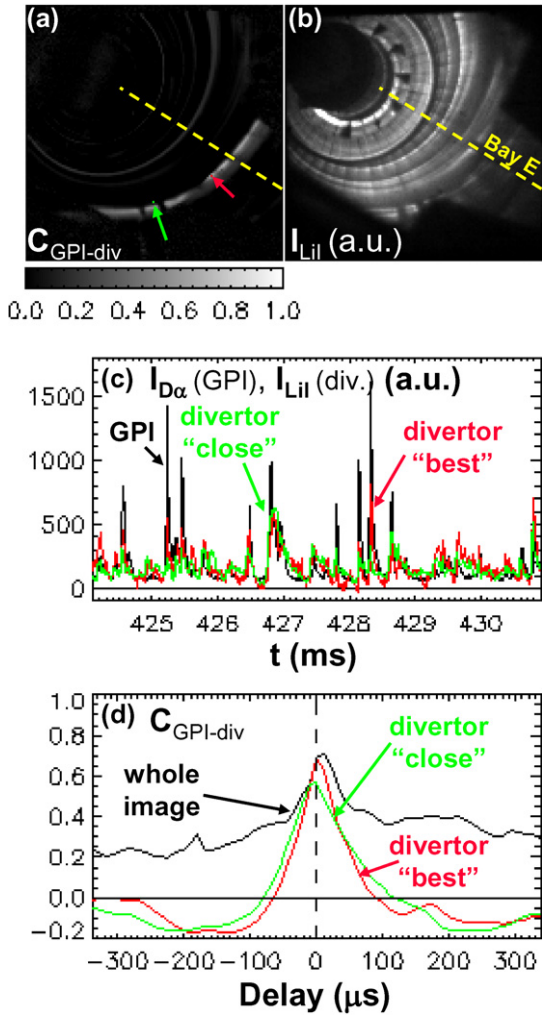


**Figure 9.** Correlation between the divertor images and the midplane GPI diagnostic. (*a*) Zero-time-lag correlation map relative to the set of pixels of GPI image indicated with a green square in figure 8(*b*). This square maps along the corresponding magnetic field line to the point indicated with a green arrow. The red arrow indicates the position where the best zero-time-lag correlation is achieved. (*b*) Reference image, same shot and time as frame #9 of figure 8(*b*), the centre of bay E is indicated with a dashed yellow line. (*c*) Raw traces from individual pixels of the GPI and divertor images, showing good correlation in the raw data. (*d*) Time delay cross-correlation between GPI and divertor.

needs to be pointed out that, when observing this black–red–green sequence at a fixed toroidal angle, this will appear to be moving inwards (the barber pole effect) in contrast to the general outward movement that midplane blobs have. The true radial movement (cyan–red–purple) seen when observing the footprint as a whole and not just limited to a narrow toroidal band is radially outwards as indicated at the beginning of this paragraph. Both of these movement features can be observed in figure 3 and the associated movie, as well as in the average filament tracks shown in figure 7.

The zero-time-lag cross-correlation between all pixels in the top-down images of the bottom divertor and a reference point in the GPI FOV, indicated with a green square in frame #9 of figure 8(*b*), is shown in figure 9(*a*). This image has the same orientation as that shown in figure 8(*c*), with the dashed yellow line indicating the centre of Bay E. A reference image of the neutral lithium emission is shown in figure 9(*b*); this image corresponds to the same shot and the same time as frame #9 in figure 8(*b*). A 1 kHz high-pass filter has been applied to all time traces before calculating the cross-correlation coefficients and an ELM-free 13 ms-long period (422–435 ms) was used for the analysis. The cross-correlation map shown in figure 9(*a*) shows an elongated region of good correlation similar to what is expected from the magnetic field-line mapping shown in figure 8(*c*). The best correlation of 68% is obtained at the pixel indicated with a red arrow, while the position of reference point in the GPI image mapped onto the divertor target is indicated with a green arrow. This divertor target point is approximately 4 m away, following the magnetic field line, from its GPI counterpart. The discrepancy observed between the red and green arrows is discussed in the following paragraph.

In figure 9(*c*) a 7 ms long portion of the time traces from the set of pixels from the GPI diagnostic indicated in frame #9 of figure 8(*b*) and two pixels from the divertor images is shown. The zero-time-lag correlation can be clearly seen in these raw signals, where only linear height transformations have been applied to the divertor traces to match the intensity and offset of the GPI trace. The red divertor trace, indicated as 'best', corresponds to the pixel where the best correlation is obtained (68% correlation). The divertor 'close', green trace corresponds to a pixel that is located in the outer divertor ∼4 cm outboard of the field-line mapped position from the GPI diagnostic. The toroidal mismatch between these two positions (green and red arrows in figure 9(*a*)) is due to the elongated character of the divertor emission structures. A small level of noise within these correlation images can generate a random toroidal displacement of the location of the best correlation. The systematic radial mismatch observed, that when mapped to the outboard midplane represents ∼1.2 cm or a variation $\Delta\Psi_N \sim 0.06$ in normalized flux function values, is possibly due to uncertainties in the localization of the separatrix and all other flux value surfaces near the midplane of the device. The cross-correlation coefficient between the midplane GPI diagnostic and the divertor 'close' position in the divertor is of 57%.

In general, as shown in figures 9(*a*) and (*c*), a good level of correlation between the divertor and the GPI diagnostic can be obtained if the magnetic mapping between the fields of view of both imaging systems is such that they 'map' into each other. This mapping condition is principally set by the magnetic field and plasma current used in the particular plasma shot. Furthermore, the best correlation is obtained with lags not exceeding ±11 $\mu$s, which represent just one inter-frame period of the cameras. As mentioned in section 2, the cameras GPI camera and the top-down viewing camera are not frame-synchronized but free running. The ±11 $\mu$s allowance for the best correlation is then still consistent with a simultaneous observation of the intermittent events at the midplane and divertor. This result is discussed in section 4 in terms of parallel propagation speeds.

The time-delayed correlation between the GPI images and the top-down divertor images is shown in figure 9(*d*). As shown here, both the divertor 'best' and divertor 'close' pixels have a well defined temporal correlation with characteristic times of several tens of microseconds. This is similar to the autocorrelation times shown in figure 5(*e*) and, also, the autocorrelation times of the midplane blobs as measured

with the GPI diagnostic [2]. When allowing for correlations between all pixels in the divertor images (black trace), the best correlation of 71% is obtained with a delay of 11 $\mu$s, but as it has been pointed out in the preceding paragraph, this delay is not significant given the hardware setup limitations. Nevertheless, in this whole image case, the good temporal cross-correlation is not as well defined as for the case of individual pixels. When allowing for earlier or later delay times, the filaments are generally located at a different position but still within the divertor FOV (cf figure 7) and, in this way, maintaining the 'whole image' time-delayed cross-correlation coefficients at an increased level for time delays away from the $\pm 11$ $\mu$s band.

In summary, from figure 9 it is clear that the midplane blobs fill up their flux tube with plasma that then interacts with the divertor plasma facing components without any measurable delay (given the current diagnostic limitations). The level of cross-correlation obtained, reaching 70% in the case shown, is remarkable given that $D_\alpha$ emission is observed in the case of the GPI diagnostic and neutral lithium emission (Li I) is measured in the case of the plasma–wall interaction in the divertor. Despite the obvious differences in the atomic physics of these two processes resulting in different functional forms for the emission rates dependence on the plasma density and temperature, it is in general an above background level of plasma interaction with neutrals that give rise to the observed visible emission. Any atomic physics difference, i.e. their detailed functional dependence on $n_e$ and $T_e$ for instance, is only a small effect in the overall plasma–neutral interaction phenomena. The large separation between the midplane and divertor ($\sim$4 m) is also a small effect in this measurement, similar to the long correlations observed in the SOL of JET, as published in [16].

### 3.3. Variation with X-point height

The correlation coefficients between the neutral lithium emission on the divertor plasma facing components and the GPI midplane diagnostic are shown in figure 10 for two shots with different X-point heights. The coefficients are calculated for all pixels within each image sequence, one sequence per shot. These pixels are then binned in terms of their major radii and the best correlation within each 2 cm-wide bin evaluated. The major radii are converted to normalized flux functions for plotting. Whereas figure 10($a$) shows the same shots as figures 8 and 9, having a low X-point and high flux expansion, figure 10($b$) shows data from shot 130316 (275–290 ms) which although being also a high elongation plasma had a higher X-point and a lower flux expansion. This flux expansion difference is then responsible for an expanded range of normalized flux function values reached in figure 10($b$) with respect to figure 10($a$). In both cases there is a region of good correlation between GPI and divertor when the GPI FOV maps into the observed divertor region. The correlation coefficients reach the 80% level in the first case and the 70% level in the second case. These correspond to a 'direct' connection path between the divertor region being observed and the GPI FOV, having a connection length of $\sim$4 m.

Another set of correlation features can be seen in figures 10($a$) and ($b$) closer to the OSP, where a reduced but still above the random-coincidence level is observed. These

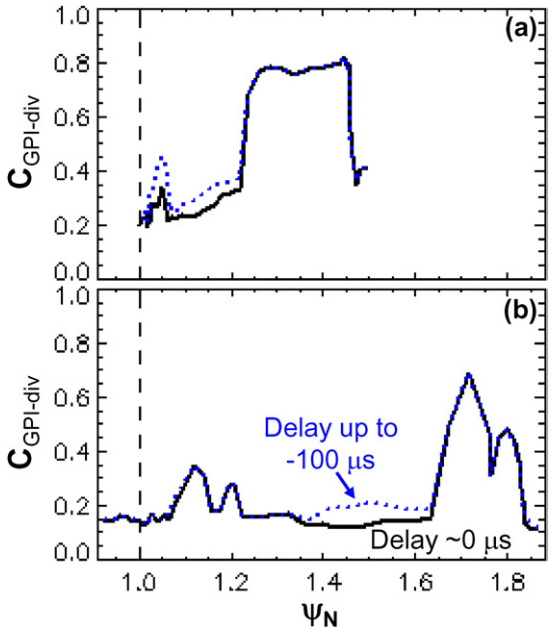


**Figure 10.** Correlation profiles between the divertor images and the midplane GPI diagnostic: ($a$) low X-point, high flux expansion shot (130322), ($b$) high X-point, low flux expansion shot (130316). In both cases they are high elongation shots with the inner strike point on the vertical section of the centre stack of NSTX. The abscissae indicate the normalized flux function based on EFIT equilibrium reconstructions. The black, solid traces correspond to the zero-time-lag correlation coefficients, the blue, dashed traces permit for a $\pm 100$ $\mu$s delay between measuring diagnostics. As in the case of figure 9, a 1 kHz high-pass filter is applied to all signals for this analysis.

correspond to flux tubes closer to the separatrix at the midplane that have wrapped once around the torus before reaching the inner divertor target plate in the area imaged by the top-down camera. The connection length between the divertor and the GPI is in the 7–8 m range. This inner correlation region is further enhanced in the case of figure 10($a$) when allowing for delays in the correlation of $\pm 100$ $\mu$s (dashed line). This increased correlation is obtained with filaments that earlier (or later) have moved out of the FOV of the top-down viewing camera and, consequently, the zero-time-lag correlation coefficient is smaller than the time-delayed correlation coefficient.

The structure of the Li I emission filaments on the inner divertor target plate can be seen also using the third, tangential camera system described in section 2. The resolution of this target plate is approximately 2.5 times better using this camera ($\sim$5 mm pixel$^{-1}$) than that obtained with the wider FOV of the top-down imaging system used earlier in this paper. This camera images the inner divertor plate out to the CHI gap (figure 11($a$)), seen in the foreground, as well as the outer divertor plate and bottom passive stabilizing plate which can be seen in the background. The separatrix shape near the X-point for these two discharges is depicted in figure 11($a$) for the two X-point heights discharges used in figure 10. Two average images are shown in figure 11($b$), on the left corresponding to a low X-point discharge (shot 130324, 424.0–436.5 ms average) and on the right a high X-point discharge (shot 130316, 275.0–290.0 ms average). The propagating filaments observed in the neutral lithium emission from the inner divertor target plate

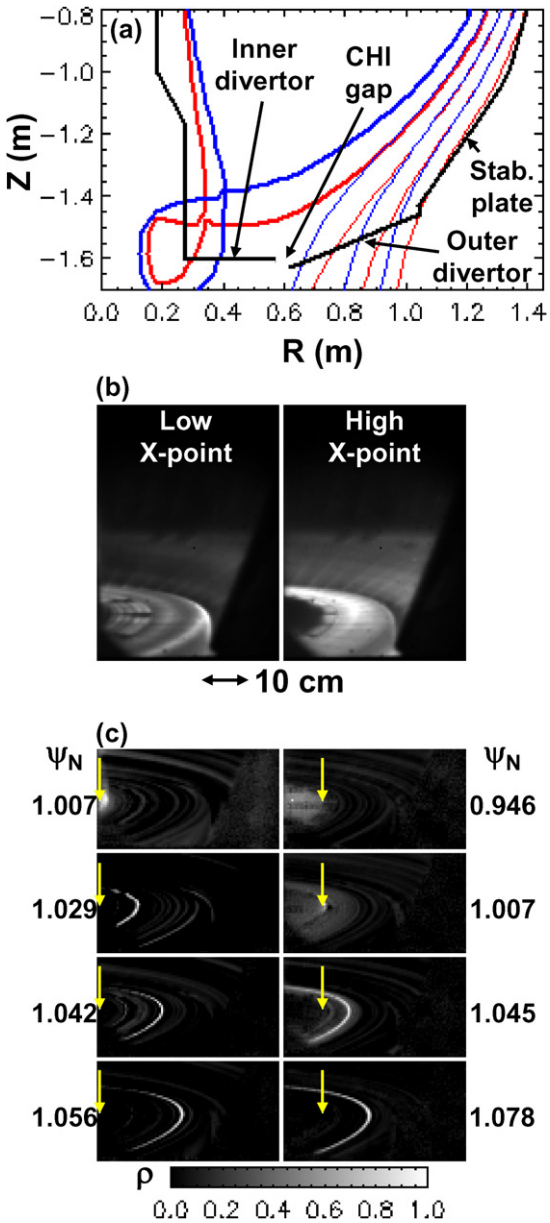


**Figure 11.** The lower divertor tangential camera has been used to observe the Li I emission from the inner target plate in low (red) and high (blue) X-point discharges, shown in (*a*). The average Li I emission in these two cases is shown in (*b*); with the inner divertor target plate and CHI gap in the foreground and the outer divertor target plate in the background. The structure of the cross-correlation maps relative to an individual pixel located on the inner target plate is shown in part (*c*). The low X-point discharge is shown in the left column and the high X-point discharge is in the right column. The position of the OSP is indicated with arrows.

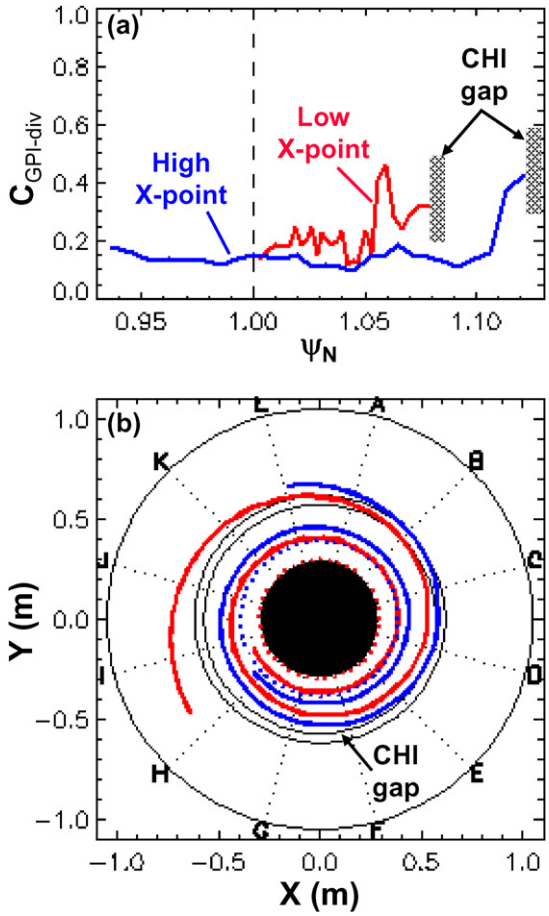


**Figure 12.** Correlation between the filaments seen with the lower divertor tangential camera and those measured with the GPI diagnostic. In (*a*) two discharges are shown, these are the low X-point (red) and the high X-point (blue) discharges also shown in figure 11. No correlation is seen close to the OSP ($\Psi_N = 1$), even though near-separatrix midplane blob should produce footprints spiralling around the centre column of NSTX as shown in (*b*). In this figure, similar to figure 8(*c*), the dotted lines in (*b*) indicate the radii of the OSP.

can be seen in the *movie*[4] covering 4 ms of discharge 130324 (431 to 435 ms). In this movie, filaments can be seen, similar to those shown earlier in figure 3, covering the inner divertor plate, outer divertor plate and lower stabilizing plate.

The structure of the fluctuations on the lower divertor target plate, filtered to 1 kHz and higher frequencies, can be seen in figure 11(*c*). These represent the zero-time-lag cross-correlation maps to reference points located at different major radii on the target plate. These radii, although at the same position in space, correspond to different normalized flux function values for the low X-point, high flux expansion case (left column) and the high X-point, low flux expansion case (right column). Several features are observed in figure 11(*c*). Away from the OSP radius, indicated with arrows, thin correlation regions are observed. Nevertheless, close to the strike point (i.e. $\Psi_N = 1.007$), no such correlation structures are found. The same applies, in the case of the high X-point case, to the private flux region (top right map in figure 11(*c*)) where only a diffuse region with an intermediate value for the correlation coefficient is observed.

The correlation between the filaments observed with the lower divertor tangential camera and the GPI diagnostic is shown in figure 12(*a*). This figure, similar to figure 10, shows the level of correlation for the two shots shown in figure 11, i.e. a low X-point, high flux expansion discharge (red trace) and a high X-point, low flux expansion discharge (blue trace). In both cases, in a similar way as figure 10, no correlation above the random-coincidence level is observed close to the OSP ($\Psi_N = 1$). In the case of the low X-point this correlation is lost inside $\Psi_N \sim 1.05$ and in the case of the high X-point inside $\Psi_N \sim 1.11$, just inside the CHI gap. As shown in figure 12(*b*),

[4] http://www.pppl.gov/~rmaqueda/other/temp/paper/nstx_movie_02.avi (18 Mbytes).

a midplane blob filament close to the separatrix would produce a divertor footprint that spirals around the centre column of NSTX. In the case of figure 12(*b*), the midplane filaments blobs mapped down to the divertor had 3 cm diameters and were centred at $\Psi_N \sim 1.12$ for the low X-point case (red) and $\Psi_N = 1.08$ for the high X-point case (blue). Despite the $\Psi_N \geqslant 1.05$ filaments in the first case (or $\Psi_N \geqslant 1.11$ in the second case) having correlations above the 40% level as shown in figure 12(*a*), no correlation is seen with the portion of the spiral that maps closer to the OSP than these normalized flux function values.

Two more observations can be made. In the first place, a careful analysis of the autocorrelation maps in figure 11 shows that the structures of the high correlation regions close to the OSP are consistent with a circular and not a spiral shape. This indicates that, although fluctuations with frequencies above 1 kHz are seen at small $\Psi_N$ values, these might correspond to local, toroidally symmetric, X-point or divertor region instabilities [26–27] and not to the extension of toroidally/poloidally elongated structures reaching the outer midplane of the device. Second, when observing the filaments in motion like in the linked movie[5], it can be seen that a difference is observed between structures close to the CHI gap which rotate toroidally in a similar way to the analysis shown in figure 7 and filaments close to the OSP do not appear to be rotating. This once more points to a different character between the structures close to the OSP and those further out in radius.

## 4. Summary and discussion

Filamentary, moving structures are seen in Li I light on the lower divertor target plates and the lower stabilizing passive plate of NSTX. These structures have intermittent characteristics with their skewness and kurtosis above those of a normal distribution. In addition, their autocorrelation time function shows no long term correlations indicating that these filaments do not correspond to long lasting periodic modes, i.e. turbulence. Furthermore, there is a good correlation between midplane GPI $D_\alpha$ and divertor Li I light fluctuations, reaching 80%, when the magnetic topology is such that the observed region of the lower divertor maps along field lines to the FOV of the GPI diagnostic located just above the outer midplane. This then indicates that the midplane blobs observed in NSTX and many other experimental devices can reach the divertor target plates as they propagate radially and poloidally/toroidally in the low-field-side SOL.

One remarkable characteristic of the correlation between the divertor filaments close to the target plates and the midplane blobs is that no delay is observed in this correlation. In all cases with good field-line mapping, the best correlation coefficients are obtained with delays of no greater than $\pm 11\,\mu$s. Under the limitations of the current diagnostic capabilities this is consistent with a near-simultaneous appearance of the intermittent events at both places as seen in other experimental devices [16]. It should be noted that the ion transit time from midplane to divertor, governing ambipolar diffusion processes, is for the case of NSTX's blobs in the range 50–100 $\mu$s. Such delay should be clearly discernable under the current diagnostic limitations.

At the same time, the characteristic time in NSTX for the propagation of potential perturbations along field lines [28] is only a fraction of a microsecond. In the case of midplane blobs with $n_e \sim 3 \times 10^{13}\,\mathrm{cm}^{-3}$ and $T_e \sim 30\,\mathrm{eV}$ (and $L_{perp} \sim 4\,\mathrm{cm}$ and $B_{edge} \sim 3.5\,\mathrm{kG}$) the diffusion of potential perturbations along field lines is characterized by a diffusion coefficient $D_\varphi \sim 4\,\mathrm{cm}^2\,\mathrm{s}^{-1}$ and then, for a parallel connection length $L_\parallel \sim 400\,\mathrm{cm}$, results in a characteristic potential propagation time of $\tau_\varphi \sim 0.4\,\mu$s. This fast potential propagation can produce the simultaneous ejection and movement of the flux tube filament along the whole outer edge of the plasma. In this case, then, parallel transport processes need to fill a short section of the parallel transit length between the area just above the X-point region and the divertor target plate.

Nevertheless, there still remains the possibility that electron thermal conduction along the flux tube is responsible for the appearance of the enhanced neutral lithium emission observed at the target plate. This fast thermal conduction can occur within timescales that are not discernable by the current imaging system. Under this scenario, a 'transport hole' near the midplane can be responsible for filling up the magnetic flux tubes with the required energy density for visible light emission to be seen shortly after some distance away, i.e. at the divertor target plates. If this is the case, it is an increase in $T_e$ rather than $n_e$ the cause of the increased Li I emission. However, it should be noted that as described in section 2 the neutral lithium emission is largely insensitive to changes in $T_e$ within the short timescales involved.

The results shown in this paper have another potential implication, affecting the radial blob propagation models. It has been proposed by Myra and co-workers that different regimes restrict the charge separation with the blob filaments [11]. This charge separation is what results in the radial movement of the blob though $\boldsymbol{E} \times \boldsymbol{B}$ drifts. One important aspect of this regime analysis is the presence or not of sheaths at the ends of blob flux tubes, or in its alternative, the end being for instance due to resistive ballooning unstable regions near the X-points. In the case of NTSX's midplane blobs, they are nominally located between the boundary of the sheath-connected regime and the resistive X-point regime [29]. As shown earlier in this paper, at least at some distance from the OSP, the blob filaments reach the divertor target plates where sheaths are present and hence provide a low resistivity path to close the flux tube and limit the charge separation (and radial velocity).

One final aspect to point out from the work presented in this paper is the absence of correlation with the midplane measurements close to the OSP radius, as shown in figures 10 and 12(*a*). The shear in the magnetic field, enhanced by the presence of the X-point [30], is responsible for the deformation of the flux tubes populated by excess plasma (blob) away from this region. Cohen and Ryutov have postulated that if such flux tube squeezing is of the order of the ion gyro-radius, the identity of the plasma tube is lost, being smaller than the space that particles within it need to occupy in their gyro-motion. As such, turbulence from the midplane can be decoupled from the divertor region and vice versa [31]. In the case of the flux tubes depicted in figure 12(*a*) these are squeezed down to ∼4 mm

[5] See footnote 4.

widths (slightly smaller for the case of the high X-point case). Nevertheless, most of the toroidally elongated footprint and, particularly in the long spiral at smaller major radii, has widths smaller than these maxima. The inner section of the spiral is, for this reason, limited to some extent by the conjectures of Cohen and Ryutov. The experimental results shown give support to this model, although not quite quantitative at this point.

In this paper we do not give any characteristics of the plasma that produce the neutral lithium emission being observed. Nor are we able to present the characteristics of the heat deposition onto the divertor surfaces due to this plasma–wall interaction. Both of these aspects could be of relevance for the protection of divertor plasma facing components in future experimental devices. As a point of reference, midplane blobs during H-modes in NSTX are estimated to have densities $n_e \leqslant 5 \times 10^{18}\,\mathrm{m}^{-3}$ and temperatures $T_e \leqslant 50\,\mathrm{eV}$. These blob filaments travel radially outwards both at the midplane and the divertor reaching components that may not be armoured for the influx of energy and particles. In the same way that intermittent events produce wider than expected density profiles in the midplane SOL, they may also contribute to the retention of tritium within co-deposited layers in divertor surfaces away from the main strike point region area. In NSTX a new set of divertor probes have been recently installed, capable of resolving features at the timescales of the fluctuating filaments. These probes will be used to characterize the plasma reaching the material surfaces as the intermittent features move by them. This will also provide a first estimate of the short timescale power fluxes to the divertor target plates.

## Acknowledgments

RJM thanks S.J. Zweben from PPPL for his support and discussions, S.A. Sabbagh from Columbia University for the EFIT equilibrium reconstructions, S.D. Loch from Auburn University for his help with ADAS data and J.R. Myra and D.A. D'Ippolito from Lodestar Research Corp. for useful discussions.

This work is supported by US DOE under grants DE-FG02-04ER54767 and DE-AC-09CH11466.

AQ3

## References

[1] Terry J.L. *et al* 2003 *Phys. Plasmas* **10** 1739
[2] Zweben S.J. *et al* 2004 *Nucl. Fusion* **44** 134
[3] Boedo J.A. *et al* 2001 *Phys. Plasmas* **8** 4826
[4] Antar G.Y., Counsell G., Yu. Y., LaBombard B. and Devynck P. 2003 *Phys. Plasmas* **10** 419
[5] Ben Ayed N., Kirk A., Dudson B., Tallents S., Vann R.G.L., Wilson H.R. and the MAST team 2009 *Plasma Phys. Control. Fusion* **51** 035016
[6] Kurzan B., Fuchs C., Scarabosio A., Scott B.D. and ASDEX Upgrade team 2009 *Plasma Phys. Control. Fusion* **51** 065009
[7] Silva C., Gonçalves B., Hidalgo C., Pedrosa M.A., Fundamenski W., Stamp M., Pitts R.A. and JET-EFDA contributors 2009 *J. Nucl. Mater.* **390–391** 355
[8] Tanaka H., Ohno N., Asakura N., Tsuji Y., Kawashima H., Takamura S., Uesugi Y. and the JT-60U team 2009 *Nucl. Fusion* **49** 065017
[9] LaBombard B., Boivin R.L., Greenwald M., Hughes J., Lipschultz B., Mossessian D., Pitcher C.S., Terry J.L. and Zweben S.J. 2001 *Phys. Plasmas* **8** 2107
[10] Krasheninnikov S.I. 2001 *Phys. Lett.* A **283** 368
[11] Myra J.R. and D'Ippolito D.A. 2005 *Phys. Plasmas* **12** 092511
[12] Ono M. *et al* 2000 *Nucl. Fusion* **40** 557
[13] Kirk A. *et al* 2007 *Plasma Phys. Control. Fusion* **49** 1259
[14] Antar G.Y., Counsell G., Ahn J.-W., Yang Y., Price M., Tabasso A. and Kirk A. 2005 *Phys. Plasmas* **12** 032506
[15] Ohno N., Masuzaki S., Miyoshi H., Takamura S., Budaev V.P., Morisaki T., Ohyabu N. and Komori A. 2006 *Contrib. Plasma Phys.* **46** 692
[16] Thomsen H., Endler M., Bleuel J., Chankin A.V., Erents S.K. and Matthews G.F 2002 *Phys. Plasmas* **9** 1233
[17] Rudakov D.L. *et al* 2005 *Nucl. Fusion* **45** 1589
[18] Kugel H.W. *et al* 2008 *Phys. Plasmas* **15** 056118
[19] Raman R. *et al* 2006 *Phys. Rev. Lett.* **97** 175002
[20] Maqueda R.J. *et al* 2003 *Rev. Sci. Instrum.* **74** 2020
[21] Stotler D.P., LaBombard B., Terry J.L. and Zweben S.J. 2003 *J. Nucl. Mater.* **313–316** 1066
[22] Roquemore A.L., Biewer T., Johnson D., Zweben S.J., Nishino N. and Soukhanovskii V.A. 2004 *Rev. Sci. Instrum.* **75** 4190
[23] Loch S.D., Colgan J., Witthoeft M.C., Pindzola M.S., Ballance C.P., Mitnik D.M., Griffin D.C., O'Mullane M.G., Badnell N.R. and Summers H.P. 2006 *At. Data Nucl. Data Tables* **92** 813
[24] Carolan P.G. and Piotrowicz V.A. 1983 *Plasma Phys.* **25** 1065
[25] Sabbagh S.A. *et al* 2001 *Nucl. Fusion* **41** 1601
[26] García-Cortés I., Hidalgo C., Martín-Solís J.R., Ali-Arshad S., Clement S., Davies S.J., Lingertat J., Loarte A., Matthews G.F. and Monk R.D. 1996 *Plasma Phys. Control. Fusion* **38** 2051
[27] Moyer R.A., Lehmer R., Boedo J.A., Watkins J.G., Xu X., Myra J.R., Cohen R., D'Ippolito D.A., Petrie T.W. and Schaffer M.J. 1999 *J. Nucl. Mater.* **266–269** 1145
[28] Terry J.L., Zweben S.J., Umansky M.V., Cziegler I., Grulke O., LaBombard B. and Stotler D.P. 2009 *J. Nucl. Mater.* **390–391** 339
[29] Myra J.R., D'Ippolito D.A., Stotler D.P., Zweben S.J., LeBlanc B.P., Menard J.E., Maqueda R.J. and Boedo J. 2006 *Phys. Plasmas* **13** 092509
[30] Farina D., Pozzoli R. and Ryutov D.D. 1993 *Nucl. Fusion* **33** 1315
[31] Cohen R.H. and Ryutov D.D. 1997 *Nucl. Fusion* **37** 621

**QUERIES**

**Page 1**
AQ1
Please be aware that the colour figures in this article will only appear in colour in the web version. If you require colour in the printed journal and have not previously arranged it, please contact the Production Editor now.

**Page 6**
AQ2
Please note that there is reference to colour in captions of figures 7– 9, 11 and 12 and in text. Please rephrase the text if you do not require colour in the print version.

**Page 12**
AQ3
Please check the details for any journal references that do not have a blue link as they may contain some incorrect information. Pale purple links are used for references to arXiv e-prints.

The Princeton Plasma Physics Laboratory is operated
by Princeton University under contract
with the U.S. Department of Energy.

Information Services
Princeton Plasma Physics Laboratory
P.O. Box 451
Princeton, NJ 08543

Phone: 609-243-2245
Fax: 609-243-2751
e-mail: pppl_info@pppl.gov
Internet Address: http://www.pppl.gov